IET Electric Power Applications

Research Article

IET Journals
The Institution of Engineering and Technology

Optimal design and control of a new permanent magnet AC contactor with forced breaking mechanism

ISSN 1751-8660
Received on 22nd February 2019
Revised 25th July 2019
Accepted on 29th August 2019
E-First on 10th January 2020
doi: 10.1049/iet-epa.2019.0193
www.ietdl.org

Liang Shu[1], Sheng Zhao[1] ✉, Ziran Wu[1], Wei Chen[1], Marcelo J. Dapino[2]

[1]*The Key Laboratory of Low-Voltage Apparatus Intellectual Technology of Zhejiang, Wenzhou University, Xueyuan Middle Road 276, 325027 Wenzhou, People's Republic of China*

[2]*Department of Mechanical and Aerospace Engineering, The Ohio State University, Columbus, OH 43210, USA*

✉ *E-mail: zs_sea501@wzu.edu.cn*

Abstract: This study addresses the design of a new type of permanent magnet contactor, which uses forced breaking to overcome failure conditions. A multi-objective optimisation method based on the genetic algorithm is used to design the contactor considering the effects of average closing time, average breaking time, impact energy, Joule heat and contactor volume. Four prototypes have been fabricated according to the optimised parameters. A control circuit is developed to increase breaking reliability. The circuit is designed as two separate modules: a normal working module and a protection module. The former is used during the normal contactor operation and the latter is used for forced breaking protection. Breaking failures are detected by comparing the time delay between the breaking control voltage and the auxiliary contact voltage. A durability experiment has been conducted to verify the protection function of the proposed PM contactor. Experimental results show that the normal working module fails to break the contactor in the last testing cycle. However, under the actuation of the protection mechanism, the contactor is forced to break and the power circuit can be successfully switched off.

1 Introduction

A permanent magnet (PM) is capable of creating a magnetic field without consuming extra electric energy. This property enables the possibility of designing electromagnetic devices with high-energy efficiency [1–3]. Electrical contactors are electrically controlled devices used for switching electrical power circuits [4]. When PMs are used to generate holding forces when the contactors are in the closed state, no excitation current is needed to maintain the electrical contact [5, 6]. Both temperature increase and noise can be substantially reduced [7–9] as summarised in Table 1.

PM contactors have been extensively studied [10–15]. The field distribution of the PM was investigated in [16] by using the 2D finite element method. The coupling among the PM, control circuit and mechanical motion was computed with Matlab software. Magnetic circuit designs were reported in [9, 17]. A 3D finite element model was developed to analyse the operating characteristics of the electromagnet with PM in [17]. In [9], an optimisation design procedure and an intelligent control method were presented for the PM contactor. Of note, a genetic algorithm (GA) was used to optimise the design parameters of the magnetic circuit.

In order to reduce the tendency of PM contactors to bounce, different control strategies and control circuits have been developed. A hardware-based electronic control unit was designed in [14] to control the making and breaking operations of a PM contactor by using charging and recharging techniques. In [18], a sensorless control method was developed to improve the closing process of a PM contactor. The position and speed of the moving armature were calculated by using only the current and voltage values of the electromagnetic coil. The closed-loop control was carried out without a displacement sensor. In [19], the dynamic behaviour of a PM contactor was investigated with and without the current-feedback control. Experimental results showed that the control system with current feedback could achieve better performance than the system without current feedback. These methods are effective to improve the dynamic characteristics of PM contactors. In these designs, the making and breaking operations of the PM contactors fully depend on the hardware-based control unit. In the closed state, the holding force is generated by the PM. When the contactor needs to break, a repulsive control voltage is generated in the control unit. The PM will be demagnetised by the demagnetisation current in the electromagnetic coil and the contactor will return to the open state under the actuation of reaction springs. However, if the control unit fails to generate the demagnetisation current due to power supply failure or coil fault, the PM contactor will remain closed. In such circumstances, the PM contactor would lose the ability to break the main circuit and a serious failure condition would occur. In [6], a PM actuator was developed in which the attraction force produced by the PM was designed to be smaller than the reaction force. If failure occurs, the contactor can be returned to the open state by the reaction force. However, in this design, the contactor requires an excitation current to be maintained in the closed state, which negatively affects the energy consumption of the system. Another PM contactor was reported in [20, 21]. An inter-locking mechanism was developed to avoid unexpected closing of the magnetic actuator. However, this design cannot be used to solve the breaking failure problem.

In order to solve the breaking failure problem, we have developed a new PM contactor with a forced breaking mechanism. If the contactor cannot break effectively, the breaking failure will be detected by a protection module and the contactor will be forced to break. This design has critical safety advantages over previous approaches. The multi-objective optimisation method is used to design the contactor considering the influences of average closing time, average breaking time, impact energy, and contactor volume. In order to avoid power supply failure, the power supply to the protection module is selected as the 380 V line voltage of the contacts. Experiments are conducted to verify the protection function of the proposed PM contactor.

Table 1 Advantages of PM contactors over conventional devices

	PM contactors	Conventional
energy consumption, VA	0.5–1	5–250
noise, dB(A)	0–5	20–40
temperature rise, K	5–10	35–60

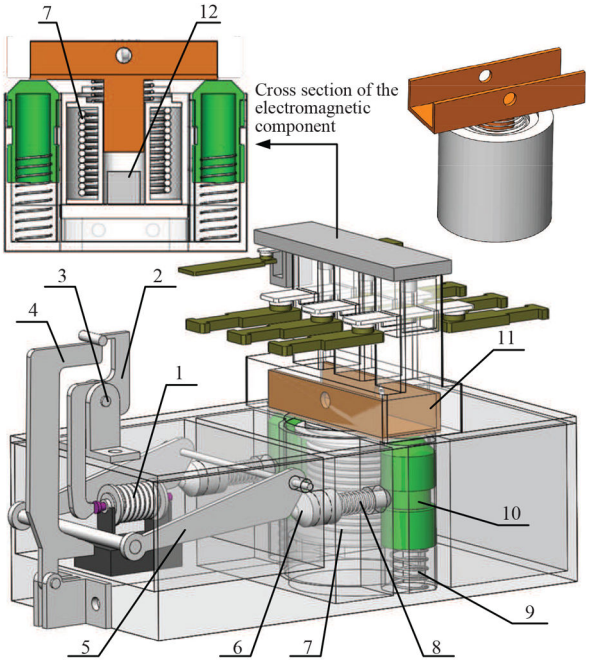

1 -Actuator, 2-Blocking bar, 3-Axis A, 4-Transmission lever, 5-Blocking lever, 6-Locking bolt, 7 - Electromagnetic coil, 8 -Bolt spring, 9-Breaking spring, 10-Blocking bolt, 11-Moving core, 12-PM.

Fig. 1 *Structure of the PM contactor*

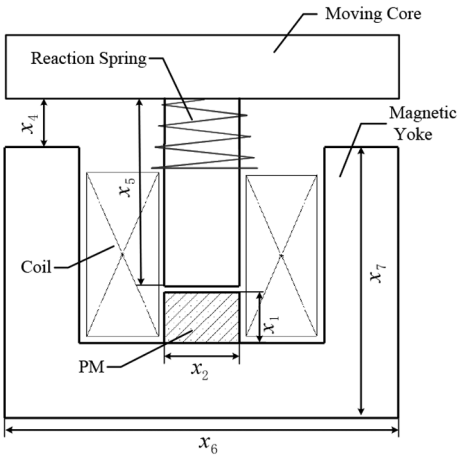

Fig. 2 *Simplified geometry of the electromagnetic component*

2 Structure design

The structure of the contactor is illustrated in Fig. 1. There is a breaking spring at either side of the coil. To provide emergency protection, the two springs are first pre-compressed either by hands or using a motorised fixture. After pre-compression, the two springs are blocked with two bolts. In this design, the breaking springs stay out of the way and do not interfere with the closing process. The springs only work when the contactor encounters a breaking failure. For normal breaking, a repulsive voltage is generated from the control unit and a voltage is applied to the electromagnetic coil. The PM is demagnetised due to the demagnetisation current in the coil. Consequently, the holding force applied by the PM disappears and the contactor returns to the open state. If the control unit fails to break the contactor, the failure is detected by the protection module and the actuator is triggered. The blocking bar rotates clockwise around the axis A under the action of the actuator. Thus, the transmission lever and the block lever are released. There are two locking bolts used in the mechanism to prevent motion of the blocking bolts. Once the resistance is removed, the breaking springs are released and the contactor is forced to break. In this way, the protection mechanism ensures that the contactor can break effectively even if failure happens to the control unit. If there is no failure, the protection mechanism remains idle, consuming no energy.

3 Multi-objective optimisation

3.1 Objective functions

The electromagnetic components of Fig. 1 can be simplified as shown in Fig. 2. Multi-objective design optimisation of the PM contactor must ensure that the closing operation is fast but with the limited mechanical impact. The stiffness and pre-compression of the breaking springs must therefore be optimised. In addition, the PM contactor is used to switch the electric devices frequently and the thermal effect of the coil design needs to be considered. To reduce manufacturing costs, the volume of the structure must be minimised. Mathematically, the optimisation is formulated by considering a vector of the form

$$\boldsymbol{X} = [x_1, x_2, x_3, x_4, x_5, x_6, x_7, x_8, x_9, x_{10}, x_{11}], \tag{1}$$

where x_1 denotes the height of the PM, x_2 is the diameter of the PM, x_3 is the compression of the breaking spring, x_4 is the distance between the moving core and the yoke, x_5 is the height of the moving core, x_6 is the outer diameter of the yoke, x_7 is the height of the yoke and x_8 is the stiffness of the breaking spring, x_9 is the excitation current, x_{10} is the coil width and x_{11} is the wire radius. To obtain a uniform field distribution inside the coil, the coil height is the same as the inner height of the yoke. Four objectives are chosen for the multi-objective optimisation: structure volume, strike energy, Joule heating power and closing time. The electromagnetic component of the PM contactor is a cylinder structure and the volume can be calculated as

$$V_{\mathrm{m}}(\boldsymbol{X}) = \pi\left(\frac{x_6}{2}\right)^2 x_7. \tag{2}$$

According to the energy conservation law

$$\int_{x_0}^{x} F_{\mathrm{m}}(\boldsymbol{X})\mathrm{d}x = \frac{1}{2}k_{\mathrm{b}}x_{\mathrm{m}}^2 + E_1(\boldsymbol{X}), \tag{3}$$

where $E_1(\boldsymbol{X})$ is the strike energy, $F_{\mathrm{m}}(\boldsymbol{X})$ is the combined electromagnetic force generated by the PM and the coil, x_{m} is the moving core displacement and k_{b} is the stiffness of the reaction spring. The strike energy $E_1(\boldsymbol{X})$ can be solved as

$$E_1(\boldsymbol{X}) = \int_{x_0}^{x} F_{\mathrm{m}}(\boldsymbol{X})\mathrm{d}x - \frac{1}{2}k_{\mathrm{b}}x_{\mathrm{m}}^2. \tag{4}$$

It is seen in (4) that the electromagnetic force $F_{\mathrm{m}}(\boldsymbol{X})$ needs to be identified to obtain $E_1\boldsymbol{X}$. Equivalent magnetic circuit analysis is used to identify $F_{\mathrm{m}}(\boldsymbol{X})$. The equivalent magnetic circuit of Fig. 2 is shown in Fig. 3, in which $\mathfrak{R}_{\mathrm{m}}$ is the equivalent magnetic resistance of the PM, $\mathfrak{R}_{a1}$, $\mathfrak{R}_{a2}$ and $\mathfrak{R}_{a3}$ are the air gap reluctances, $\mathfrak{R}_{p1}$, $\mathfrak{R}_{p2}$ and $\mathfrak{R}_{p3}$ are the reluctances of the moving core, $\mathfrak{R}_{s1}$, $\mathfrak{R}_{s2}$, $\mathfrak{R}_{s3}$ and $\mathfrak{R}_{s4}$ are the reluctances of the static core and the yoke, H_{c} is the magnetic coercive force, i is the excitation current, N_{c} is the coil turns per metre and h_{m} is the thickness of the PM. The interior magnetic resistance of the PM can be expressed as

$$\mathfrak{R}_{\mathrm{m}} = \frac{F_\psi}{\phi} = \frac{H_{\mathrm{c}}h_{\mathrm{m}}}{B_{\mathrm{r}}S} = \frac{H_{\mathrm{c}}x_1}{B_{\mathrm{r}}\pi(x_2/2)^2}, \tag{5}$$

where F_ψ is the magnetomotive force of the PM, ϕ is the flux in the magnetic path, B_{r} is the PM remanence and S is the cross area of the PM. The cross area of the magnetic path is the same. By using the definition of the parameter vector $\boldsymbol{X}$, the reluctances of the moving core, the magnetic yoke and the static core can be calculated as

$$\mathfrak{R}_{a1} = \mathfrak{R}_{a2} = \mathfrak{R}_{a3} = \frac{x_4}{\mu_0 \pi (x_2/2)^2}, \tag{6}$$

$$\mathfrak{R}_{s1} = \mathfrak{R}_{s2} = \frac{x_7}{\mu_0 \mu_r \pi (x_2/2)^2}, \tag{7}$$

$$\mathfrak{R}_{p1} = \mathfrak{R}_{p2} = \mathfrak{R}_{s3} = \mathfrak{R}_{s4} = \frac{(1/2)x_6}{\mu_0 \mu_r \pi (x_2/2)^2}, \tag{8}$$

where μ_0 is the permeability of the free air. The magnetic path consists of solid #10 magnetic steel (AISI 1010 equivalent). Eddy current losses can be omitted since the contactor is excited with constant current and the duration of the current is very short. To consider the nonlinearity of the relative permeability μ_r, we assume the ratio between the flux density and the field is described by the Froëlich equation [22]:

$$B = \frac{aH}{1 + bH}, \tag{9}$$

where the parameters a and b are identified from the experimental data. After identification, the values $a = 0.001$ and $b = 0.0006$ are used. The parallel reluctance in Fig. 3 can thus be written as

$$\mathfrak{R}_{\text{pal}} = \frac{1}{2}(\mathfrak{R}_{p1} + \mathfrak{R}_{a1} + \mathfrak{R}_{s1} + \mathfrak{R}_{s3}). \tag{10}$$

The reluctance of the pole of the moving core can be calculated as

$$\mathfrak{R}_{p3} = \frac{x_5}{\mu_0 \mu_r \pi (x_2/2)^2}. \tag{11}$$

Combination of (5), (10) and (11) gives an expression for the total reluctance of the magnetic path:

$$\mathfrak{R}_{\text{tol}} = \mathfrak{R}_{\text{m}} + \mathfrak{R}_{\text{pal}} + \mathfrak{R}_{p3} + \mathfrak{R}_{a3}. \tag{12}$$

To consider the flux leakage in the magnetic path, a position-dependent coefficient k_σ is used, which is interpolated as the function of the position of the moving core and the thickness of the PM [15]:

$$k_\sigma = \frac{x_4 + x_1}{x_1}. \tag{13}$$

Thus, the flux in the moving core can be written as

$$\phi_{\text{m}} = \frac{\phi}{k_\sigma}. \tag{14}$$

According to Ampere's law

$$H_c h_{\text{m}} + N_c i = k_\sigma B_a S(\mathfrak{R}_{\text{m}} + \mathfrak{R}_{\text{pal}} + \mathfrak{R}_{p3} + \mathfrak{R}_{a3}), \tag{15}$$

where B_a is the flux density in the moving core. From (15), B_a can be solved as

$$B_a = \frac{H_c x_1 + N_c i}{(\mathfrak{R}_{\text{m}} + \mathfrak{R}_{\text{pal}} + \mathfrak{R}_{p3} + \mathfrak{R}_{a3})}. \tag{16}$$

Experimental measurements have been conducted to verify (16). A thin layer pickup coil is wound on the moving core and a Lakeshore 480 flux metre is used to measure the dynamic flux density. The bandwidth of the flux metre is 50 kHz and the sampling frequency is 100 kHz. A digital current source is used to supply the excitation current with a magnitude of 800 mA. The result is shown in Fig. 4. Since we have considered the influences of both nonlinear permeability and flux leakage, the calculated flux distribution is consistent with the measurement.

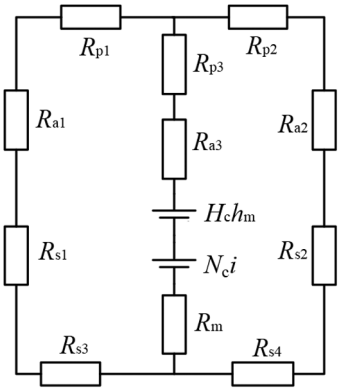

Fig. 3 *Equivalent magnetic circuit model*

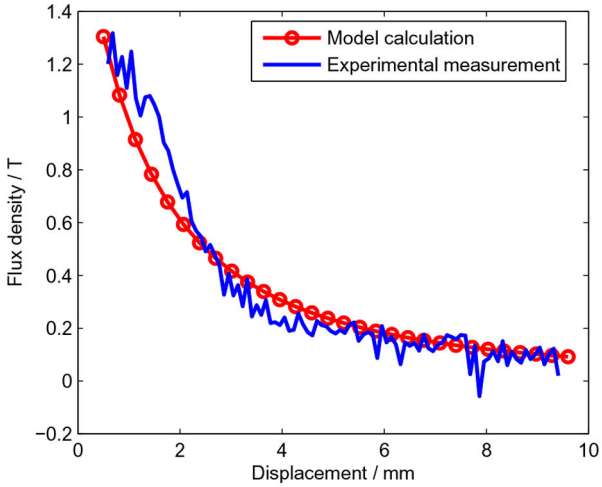

Fig. 4 *Comparison of calculated flux density with experimental measurement*

The attraction force generated by the PM and the coil can be expressed as

$$F_{\text{m}}(\boldsymbol{X}) = \frac{B_a^2 S}{2\mu_0} = \frac{B_a^2 \pi (x_2/2)^2}{2\mu_0}. \tag{17}$$

To determine the closing time of the PM contactor, the velocity of the moving core is calculated:

$$v(\boldsymbol{X}) = \sqrt{v_0^2 + 2\int_{x_0}^{x} \frac{F_{\text{m}}(\boldsymbol{X})}{M} \mathrm{d}x}, \tag{18}$$

where M denotes the mass of the moving component and v_0 is the initial velocity. Since $\mathrm{d}t(x)/\mathrm{d}x = 1/v(x)$, we have $\mathrm{d}t(x) = \mathrm{d}x/v(x)$. Then the time integration can be expressed as follows:

$$\int_{t_0}^{t} \mathrm{d}t(x) = \int_{x_0}^{x} \frac{\mathrm{d}x}{v(x)} = \int_{x_0}^{x} \frac{\mathrm{d}x}{\sqrt{v_0^2 + 2\int_{x_0}^{x} (F_{\text{m}}(\boldsymbol{X})/M)\,\mathrm{d}x}}. \tag{19}$$

So the closing time $T(\boldsymbol{X})$ can be calculated as

$$T(\boldsymbol{X}) = t = t_0 + \int_{x_0}^{x} \frac{\mathrm{d}x}{\sqrt{v_0^2 + 2\int_{x_0}^{x} (F_{\text{m}}(\boldsymbol{X})/M)\,\mathrm{d}x}}, \tag{20}$$

where t_0 denotes the initial time and x_0 is the initial position.

The Joule heat effect of the electromagnetic coil needs to be considered in the optimisation process. A cross section of the coil is shown in Fig. 5, in which each circle represents a coil turn. The coil height is denoted with l and it is considered the same as the inner height of the yoke. By using the formula of arithmetic

sequence summation, the total length of the coil wire L_t can be calculated as

$$L_t = \frac{x_{10}x_2\pi l}{4x_{11}^2} + \frac{x_{10}^2\pi l}{4x_{11}^2}. \tag{21}$$

The Joule heat power can be expressed as

$$P_h(\boldsymbol{X}) = i^2\rho\frac{L_t}{A_c} = \rho x_9^2\frac{x_{10}x_2 l + x_{10}^2 l}{4x_{11}^4}, \tag{22}$$

where A_c denotes the cross-sectional area of the wire.

3.2 Optimisation of the closing process

It has been discussed that for the multi-objective optimisation of the PM contactor, the contactor volume is expected to be small. This implies that Joule heating in the coil is limited. Also, the closing process is desired to be fast but minimal mechanical impact. The following evaluation function is constructed to implement the multi-objective optimisation:

$$f(\boldsymbol{X}) = \frac{\lambda_1 V_m(\boldsymbol{X})}{V_{m0}} + \frac{\lambda_2 E_1(\boldsymbol{X})}{E_0} + \frac{\lambda_3 T(\boldsymbol{X})}{T_0} + \frac{\lambda_4 P_h(\boldsymbol{X})}{P_{h0}}, \tag{23}$$

where V_{m0}, E_0, T_0 and P_{h0} are the initial design parameters based on an existing PM contactor, λ_1, λ_2, λ_3 and λ_4 are the weighted factors which satisfy the following equation:

$$\lambda_1 + \lambda_2 + \lambda_3 + \lambda_4 = 1. \tag{24}$$

A GA is used to minimize (23) [23, 24]. The objective is to find a vector $\boldsymbol{x}^*$ in the solution space $\boldsymbol{X}^*$ that minimises the evaluation function (23). To apply the GA, a solution vector $\boldsymbol{x}^* \in \boldsymbol{X}^*$ is encoded as a string of binary numbers called a gene. Genes are cascaded to form a longer string called a chromosome. The genetic algorithm operates with a collection of chromosomes, called a population. As the search evolves, the population includes fitter and fitter solutions, and eventually it converges to the solution $\boldsymbol{x}^*$. The flowchart of the GA is illustrated in Fig. 6.

When determining which pair of strings is selected from the current population Θ, the selection probability $P(\boldsymbol{x}_i)$ is calculated as follows:

$$P(\boldsymbol{x}_i) = \frac{f(\boldsymbol{x}_i) - f_{\min}(\Theta)}{\sum_{j=1}^{N}\left(f(\boldsymbol{x}_j) - f_{\min}(\Theta)\right)}, \tag{25}$$

where $f(\boldsymbol{x}_i)$ is the fitness of individual i, N is the population size and $f_{\min}(\Theta) = \min\{f(\boldsymbol{x})|\boldsymbol{x} \in \Theta\}$. In the optimisation of the closing process, the estimation function needs to be subjected to the following constraint conditions:

i. The permanent magnet is placed inside the magnetic yoke

$$x_1 < x_7, \quad x_2 < x_6. \tag{26}$$

ii. The height of the moving core should be less than the distance between the moving core and the stator, which is

$$x_4 < x_5. \tag{27}$$

iii. To ensure that the contactor can be closed when subjected to the excitation current, the ampere–turns product needs to be greater than minimal value, $N_c i = x_9 x_{10}/(4x_{11}^2) > F_\delta$, where $F_\delta = 4000$ is identified from the force magnitude of the reaction spring in our design.

The convergence of the objective functions in the closing process is illustrated in Fig. 7 and the optimisation results are listed in Table 2. It can be seen from Fig. 7 that the four objective functions converge to steady-state values in about 260 runs. The optimal parameters listed in Table 2 show that the closing performance of

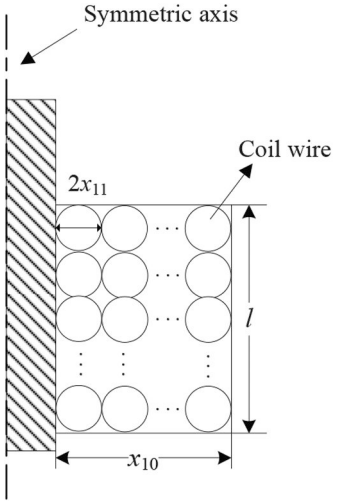

Fig. 5 *Symmetric geometry of the electromagnetic coil*

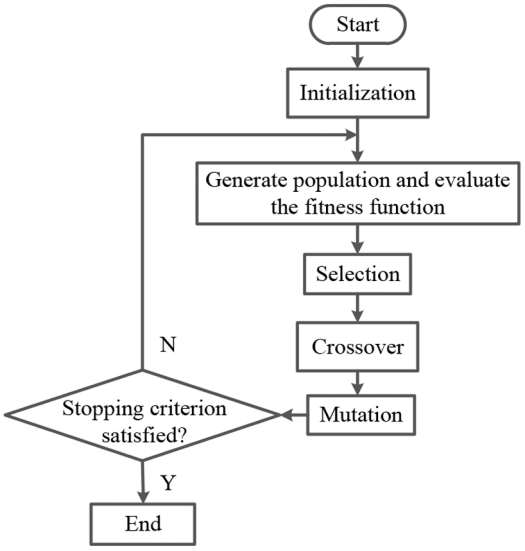

Fig. 6 *Flowchart of genetic algorithm*

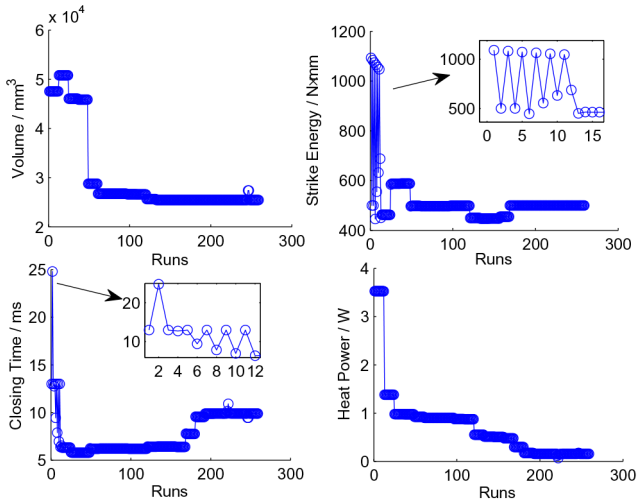

Fig. 7 *Optimisation of the objective functions (closing)*

the contactor has been improved through the optimisation process. The volume of the contactor is decreased by 46.46%, which is beneficial for reducing the manufacturing costs. The closing time has been decreased by 23% and the strike energy is decreased by 54.12%. Since a thicker wire is used, the Joule heat has been decreased by 26.8%. These optimisation results show that the

Table 2 Optimisation results of the closing process

Parameters	Initial value	After optimisation
PM height x_1, mm	4	7
PM diameter x_2, mm	12	16
distance between core and stator x_4, mm	10	12
core height x_5, mm	27	23
yoke diameter x_6, mm	40.5	30
yoke height x_7, mm	36.9	36
excitation current x_9, mA	200	893
coil width x_{10}, mm	4	4.479
wire radius x_{11}, mm	0.2	0.5
strike energy, N mm	1093	501.46
closing time, ms	13	10
volume, mm^3	47,536	25,450
joule heat, W	0.2368	0.1733

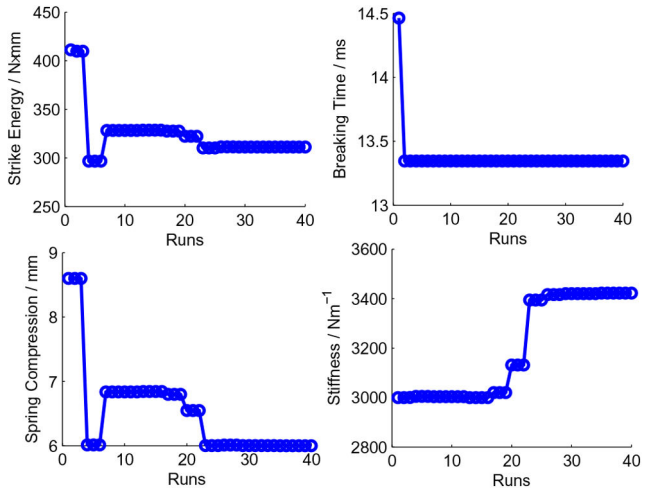

Fig. 8 *Optimisation of the objective functions (forced breaking)*

Table 3 Optimisation results of the forced breaking process

Parameters	Initial value	After optimisation
spring compression x_3, mm	8.6	6
stiffness x_8, N/m	3000	3420
strike energy, N mm	411	311.1
breaking time, ms	14.46	13.35

contactor is closing faster and the mechanical durability can be increased.

3.3 Optimisation of the forced breaking

In this section, the forced breaking process is optimised based on the optimisation results discussed in the previous section. It is noted that the behaviour of the forced breaking only depends on the spring compression x_3 and the stiffness x_8. According to the energy conservation law

$$\frac{1}{2}x_8x_3^2+\frac{1}{2}k_bx_{4c}^2=\int_{x_0'}^{x_{4c}}F_{mc}dx+E_2(\boldsymbol{X}), \tag{28}$$

where $E_2(\boldsymbol{X})$ is the strike energy in the forced breaking process and the subscript c denotes the optimised value in the previous section. The optimised hold force F_{mc} can be calculated based on (17), by taking current i as zero. The strike energy of the forced breaking can be solved as

$$E_2(\boldsymbol{X})=\frac{1}{2}x_8x_3^2+\frac{1}{2}k_bx_{4c}^2-\int_{x_0'}^{x_{4c}}F_{mc}\,dx. \tag{29}$$

It is seen from Figs. 1 and 2 that the breaking spring compression x_3 is less than the distance between the moving core and the stator x_4. The full forced breaking process can be divided into two periods. In the first period, the moving core is subjected to three external forces, the restoring force from the breaking spring, the restoring force from the reaction spring and the holding force from the permanent magnet. The total force F_{T1} can be written as

$$F_{T1}=F_r+F_b-F_{mc}\quad \text{if } x_t<x_3, \tag{30}$$

where F_r is the force from the reaction spring, F_b is the force from the breaking spring and x_t is the displacement of the moving core in the forced breaking process. By using the similar procedure of calculating the closing time $T(\boldsymbol{X})$, the forced breaking time of the first period $T_{21}(\boldsymbol{X})$ is calculated as

$$T_{21}(\boldsymbol{X})=\int_{x_0'}^{x_3}\frac{dx}{\sqrt{v_0^2+2\int_{x_0'}^{x_3}(F_{T1}/M)\,dx}} \tag{31}$$

In the second period, when x_t is larger than x_3, the anti-force from the breaking spring is zero and the moving core is only subjected to the combined force of the reaction spring and the permanent magnet. The total force F_{T2} can be calculated as

$$F_{T2}=F_r-F_{mc}\quad \text{if } x_t\geq x_3. \tag{32}$$

The forced breaking time of the second period $T_{22}(\boldsymbol{X})$ can be calculated as

$$T_{22}(\boldsymbol{X})=\int_{x_3}^{x_{4c}}\frac{dx}{\sqrt{v_0'2+2\int_{x_3}^{x_{4c}}(F_{T2}/M)\,dx}}, \tag{33}$$

where v_0' is the velocity at $x=x_3$. Thus, the total forced breaking time is

$$T_2(\boldsymbol{X})=T_{21}(\boldsymbol{X})+T_{22}(\boldsymbol{X}). \tag{34}$$

Now we construct the evaluation function as

$$f_b(\boldsymbol{X})=\frac{\beta_1E_2(\boldsymbol{X})}{E_{b0}}+\frac{\beta_2T_2(\boldsymbol{X})}{T_{b0}}, \tag{35}$$

where β_1 and β_2 are the weighted factors, and E_{b0} and T_{b0} are the initial design parameters. The same optimisation procedure developed in the previous section is used to minimise the function $f_b(\boldsymbol{X})$ and the optimisation process needs to be subjected to the following constraints:

i. The force from the breaking spring and the reaction spring needs to be greater than the holding force of the permanent magnet, which is

$$2x_8x_3+F_r>F_{mc}. \tag{36}$$

ii. The spring compression x_3 should be less than the optimised x_{4c}.

The optimisation results are shown in Fig. 8. The optimised parameter values are shown in Table 3, where the breaking time has been decreased by 7.68% and the strike energy has been decreased by 16.78%. The short breaking time is helpful to extinguish the electric arc and the small strike energy is useful to increase the mechanical durability of the system.

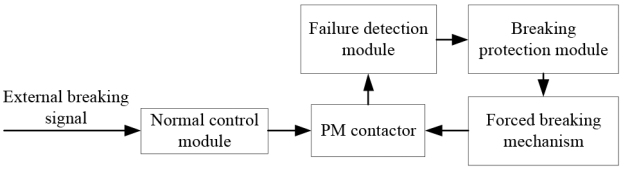

Fig. 9 *Block diagram of the controller design*

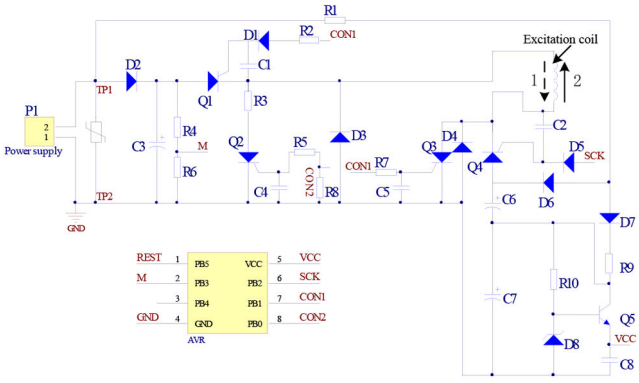

Fig. 10 *Circuit schematic of the normal control module*

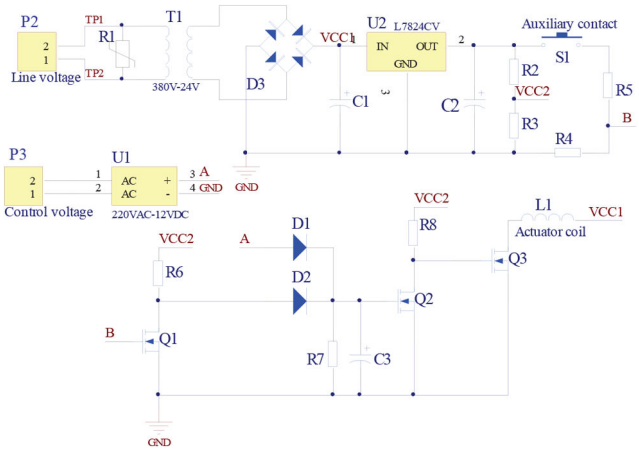

Fig. 11 *Circuit schematics of the failure detection module and the breaking protection module*

Table 4 Truth table of the logic design

Input		Output
A	*B*	*C*
0	0	0
0	1	1
1	0	0
1	1	0

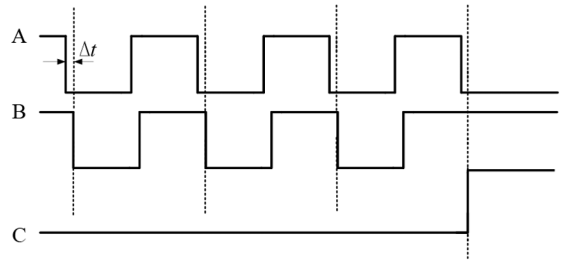

Fig. 12 *Waveform analysis chart*

4 Breaking control strategy

4.1 Control modules

There are three modules in the controller design, the normal control module, the failure detection module and the breaking protection module. The block diagram of the controller is illustrated in Fig. 9. The normal control module is used for the normal operations control of the contactor. There is a control unit embedded in the control module to supply the constant current for closing. Feedback is implemented with a current sensor. Breaking failure is detected by measuring the auxiliary contact voltage. Failure can be confirmed if this voltage remains unchanged when the breaking signal has been received. The protection module will not be triggered if the contactor breaks correctly in each operation. If a breaking failure is detected, the protection module will be activated and the contactor will be forced to break under the actuation of the forced breaking mechanism.

The circuit schematic of the normal control module is shown in Fig. 10. The power supply P1 is from the electric utility. The current direction in the excitation coil is controlled by the thyristors Q_1, Q_2, Q_3 and Q_4. When the contactor needs to close, Q_1 and Q_3 will become conducting and the direction of the current flow is marked as arrow 1. The moving core will be attracted downward by the combined force of the coil and the permanent magnet. In the opposite, if Q_2 and Q_4 are switched on, the current flow will be with the direction of arrow 2. The permanent magnet will be demagnetised and the contactor will return to the open state under the actuation of the reaction springs.

The schematics of the failure detection module and the breaking protection module are illustrated in Fig. 11. Usually the breaking failures result from a power supply failure. In order to increase the breaking reliability, the power supply to the protection module P2 is selected as the 380 V line voltage of the contacts. This design enables that the power supply always can be guaranteed as long as the contactor is in the closed state.

4.2 Control logic design

The voltage at point A in Fig. 11 is marked as the external breaking signal V_A and the voltage at point B is marked as V_B. If there is no external control signal, V_A is maintained high and the contactor is kept in the close state. If V_A is low, a breaking signal is received and the contactor needs to break instantly. V_B in Fig. 11 denotes the auxiliary contact voltage. The contactor breaks correctly if V_B is low. The contactor encounters breaking failure if V_B is high. Here we use V_C to represent the trigger voltage of the actuator coil in Fig. 11. If V_C is high, the actuator is triggered and the contactor is forced to break. The truth table of the logic controller design is shown in Table 4. It is seen from the table that the condition to trigger the actuator is $\overline{A}B$. Since $\overline{A}B = \overline{A + \overline{B}}$, so the controller can be implemented with one OR gate and two NOT gates. In Fig. 11 it is observed that one of the NOT gate is constituted by R_6 and Q_1 to obtain $\overline{B}$ at BD. The diodes of D_1 and D_2 are connected in parallel. The OR gate is implemented with D_1, D_2 and R_7 to get $A + \overline{B}$ at DQ. R_8 and Q_2 are connected with the same structure as R_6 and Q_1, and $\overline{A + \overline{B}}$ can be obtained at QQ to finally control the actuator coil.

In practice, there is a time delay between the voltages at A and B. The time sequences of the two voltages are not exactly synchronous and the time delay can be observed from Fig. 12. It is seen that there is time delay Δt between the fall edges of V_A and V_B. In this circumstance, the trigger condition $\overline{A}B$ will always be satisfied, regardless of what the real control input is. In order to solve this problem, we use an RC circuit to compensate the time delay. The RC circuit is composed of R_7 and C_3. It is seen from Fig. 11 that C_3 starts to discharge when the breaking signal is received. The thyristor Q_3 will not be conducted before C_3 is discharged to the threshold voltage. If it is detected that V_B is still high after C_3 reaches the threshold voltage, Q_3 is conducted and the actuator will be triggered (Fig. 15).

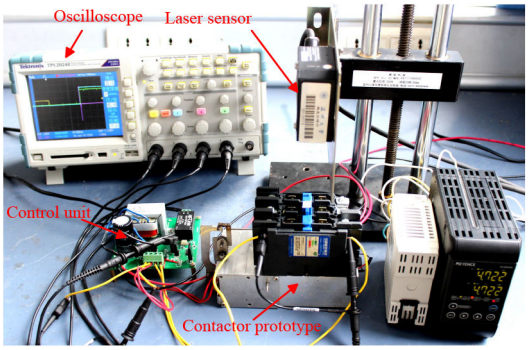

Fig. 13 *Experimental setup*

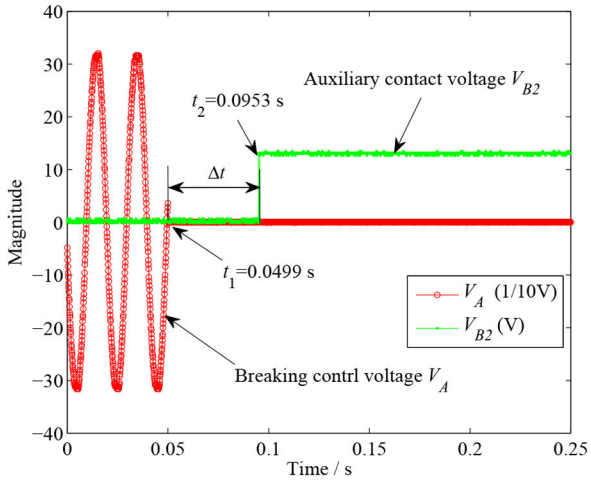

Fig. 14 *Measurement result of the time delay*

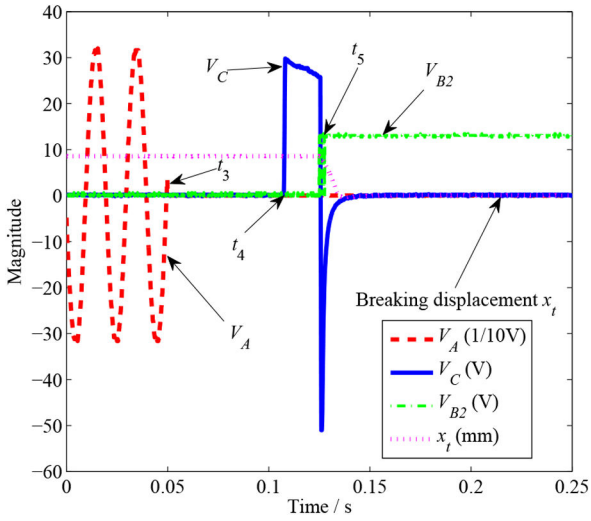

Fig. 15 *Experimental result of forced breaking*

5 Experimental research

5.1 Evaluation of the time delay circuit

In order to implement the RC circuit design, the magnitude of Δt needs to be identified. A breaking experiment is performed to investigate the value of Δt (Fig. 13). A laser sensor is used to measure the breaking displacement and an oscilloscope is used to record the measurement data. The sampling frequency is set as 50 kHz. The experimental result is shown in Fig. 14. It is noted that what we have plotted in the figure is $\overline{V_B}$ and the inverting of V_B. Here we use V_{B2} to represent $\overline{V_B}$. In order to plot V_A and V_{B2} in the same window, the magnitude of V_A has been scaled by 10. It is seen from Fig. 14 that the breaking signal is received at time $t_1 = 49.9$ ms. The auxiliary contacts break at $t_2 = 95.3$ ms. The time delay Δt is around 45.4 ms. This value is used in the RC circuit

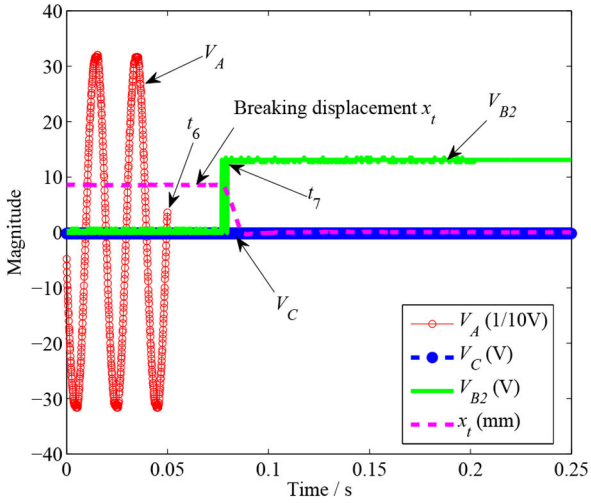

Fig. 16 *Experimental result of normal breaking*

design by considering some safety margin. The time delay is calculated according to the following equation:

$$t_{\mathrm{d}} = R_{\mathrm{d}} C_{\mathrm{d}} \times \ln\left(\frac{V_1 - V_0}{V_1 - V_t}\right), \tag{37}$$

where V_1 is the capacitor voltage after discharge, V_0 is the voltage before discharge, V_t is the capacitor voltage at time t, R_{d} is the resistance and C_{d} is the capacitance. In our design, the capacitor threshold voltage is selected as 5 V, $V_0 = 12$ V, $V_1 = 0$ V, $R_{\mathrm{d}} = 30\,\mathrm{k\Omega}$, $C_{\mathrm{d}} = 2.2\,\mu\mathrm{F}$ and the calculation result of t_{d} is 57 ms.

5.2 Comparative experiments

In order to verify the functionality of the forced protection mechanism, two groups of comparative experiments are conducted to investigate the performance of the protection module and the mechanism. In the first group, the PM contactor is in the closed state and the power supply to the normal control module is removed. Breaking results are illustrated in Fig. 15. It is seen that when the breaking signal is received at t_3 (the breaking voltage $V_A = 0$ at this point), both the capacitor voltage V_{B2} and the auxiliary contact voltage V_C are zeros. After the capacitor voltage is discharged to the threshold value, it is detected that $V_{B2} = \overline{V_B}$ is still zero. The trigger condition $\overline{A}B$ is satisfied and V_C changes to high voltage at t_4. Thereafter the voltage of V_{B2} changes to high at t_5 and the breaking displacement x_t is observed from the figure. This proves that the contactor breaks correctly even if the power supply to the control module is removed. In the second group of experiments, the contactor is kept in the closed state and the power supply is reconnected. The experimental result is shown in Fig. 16. It is seen that the breaking signal is received at t_6. The power of the normal control module has been restored and the contactor breaks correctly at t_7. This happens before the capacitor voltage discharges to the threshold value and condition $\overline{A}B$ is not satisfied. The protection mechanism is not triggered and it is observed in Fig. 16 that V_C maintains low voltage in the whole breaking process.

5.3 Verification of the emergency protection

A durability test of the proposed PM contactor is discussed in this section. This test is conducted to verify that when the contactor is in the working condition, whether the circuit still can be cut off (emergency protection) when a breaking failure happens. Four contactor prototypes have been fabricated based on the optimised parameters. According to IEC 60947-4, the prototypes are tested with a current equal to three times the rated current of 25 A. Closing and breaking cycles are applied to the contactors and the cycle numbers are recorded by a counter. The test is stopped if the contactor fails to close or the contactor is forced to break. In order

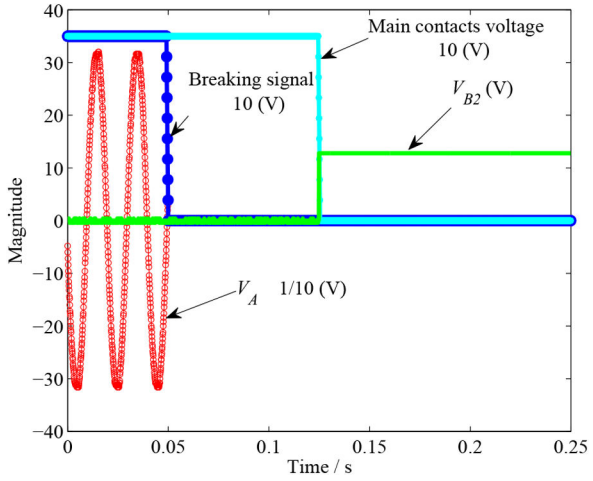

Fig. 17 *Forced breaking in the durability test*

Table 5 Durability test results of the four prototypes

No.	Test cycles	State
1	24,181	failed to close
2	13,522	failed to break, the coil is burnt, forced breaking
3	22,914	failed to break, the coil is burnt, forced breaking
4	18,291	failed to close

to measure the forced breaking behaviour in the durability test, a data acquisition unit is designed. The unit is not activated until it is triggered by a step voltage. Here we choose the actuation voltage V_C as the trigger signal and the measured result is shown in Fig. 17. It is seen from the figure that when a breaking failure happens, the main circuit still can be cut off (V_{B2} = High). These results demonstrate that the breaking failure issue exhibited by other designs has been successfully solved with the proposed design. It is emphasised that the recorded data in Fig. 17 is the last cycle of the durability test. The normal control module fails to break the contactor in the last test cycle. Under the actuation of the protection mechanism, the contactor is forced to break and the main circuit is successfully switched off by the contactor. The durability test results of the four prototypes are illustrated in Table 5. The forced breaking mechanism works successfully in the test and potential electric damages have been avoided.

6 Conclusions

A new PM AC contactor is proposed which can be forced to break if failure happens in the normal breaking process. The multi-objective optimisation is used to design the contactor. The closing and breaking performances have been improved after optimisation. A control strategy based on logic circuit design is proposed to control the protection mechanism. Experimental results show that if the normal control module works correctly, the protection module will not be activated. If the contactor encounters the breaking failure, the protection mechanism will be triggered and the contactor will be forced to break. A durability test is performed to verify the functionality of the contactor. It is seen in the test results that the protection mechanism successfully breaks the contactor in the last cycle of the durability test.

7 Acknowledgments

This work was supported in part by the National Natural Science Foundation of China under Grants nos. 51975418 and 51607123, in part by the Zhejiang Key Research and Development Program under Grant no. 2017C01008, in part by the Analytical and Testing Technology Project of Zhejiang Province under Grant no. 2018C37068, in part by the Key Technology Research Project of Wenzhou under Grants nos. 2018ZG020 and ZG2017002.

8 References

[1] Cupertino, F., Leuzzi, R., Monopoli, V.G., *et al.*: 'Maximisation of power density in permanent magnet machines with the aid of optimisation algorithms', *IET Electr. Power Appl.*, 2018, **12**, (8), pp. 1067–1074

[2] Paar, C., Muetze, A., Kolbe, H.: 'Influence of machine integration on the thermal behavior of a pm drive for hybrid electric traction', *IEEE Trans. Ind. Appl.*, 2015, **51**, (5), pp. 3914–3922

[3] Chappuis, B., Gavin, S., Rigazzi, L., *et al.*: 'Speed control of a multiphase active way linear motor based on back emf estimation', *IEEE Trans. Ind. Electron.*, 2015, **62**, (12), pp. 7299–7308

[4] Brando, G., Pizzo, A.D., Di Noia, L.P., *et al.*: 'Two-phase high-performance control of a reliable stand-alone induction generator', *IET Electr. Power Appl.*, 2017, **11**, (3), pp. 460–470

[5] Chi, C.T.: 'Applying closing phase-angle control technique in bounce reduction of AC permanent magnet contactor', *Active Passive Electron. Compon.*, 2009, **2009**, pp. 1–12, Art. ID. 609298

[6] Rong, M., Lou, J., Liu, Y., *et al.*: 'Static and dynamic analysis for contactor with a new type of permanent magnet actuator', *IEICE Trans. Electron.*, 2006, **E89-C**, (8), pp. 1210–1216

[7] Fang, S., Lin, H., Wang, X., *et al.*: 'Design and performance analysis of a vacuum permanent magnet contactor'. Proc. 14th Biennial Conf. Electromagnetic Field Computation, Chicago, IL, USA, 9–12 May 2010, Art. ID. 5481747

[8] Chi, C.T.: 'Develop a de-bounce and energy-saving characteristic ac PM contactor and its microcontroller-based electronic control unit', *JInt. J. Innov. Comput. Inf. Control*, 2010, **6**, (2), pp. 423–438

[9] Lin, H., Wang, X., Fang, S., *et al.*: 'Design, optimization, and intelligent control of permanent-magnet contactor', *IEEE Trans. Ind. Electron.*, 2013, **60**, (11), pp. 5148–5159

[10] Chi, C.T.: 'Design and implementation of a new permanent ac contactor with colenoid actuator', *WSEAS Trans. Circuits Syst.*, 2008, **7**, (11), pp. 942–954

[11] Fang, S., Lin, H.: 'Magnetic field analysis and control circuit design of permanent magnet actuator for AC contactor'. ICEMS 2005 Proc. 8th Int. Conf. Electrical Machines and Systems, Nanjing, People's Republic of China, September 2005, vol. 1, pp. 280–283

[12] Chi, C.T.: 'A high performance AC permanent magnet contactor', *WSEAS Trans. Electron.*, 2008, **5**, (7), pp. 313–322

[13] Fang, S., Lin, H., Ho, S.: 'Transient co-simulation of low voltage circuit breaker with permanent magnet actuator', *IEEE Trans. Magn.*, 2009, **45**, (3), pp. 1242–1245

[14] Chi, C.T.: 'Towards the control of a permanent magnet contactor based on charging and recharging techniques', *WSEAS Trans. Electron.*, 2008, **7**, (5), pp. 323–333

[15] Wang, X., Lin, H., Fang, S., *et al.*: 'Dynamic performance analysis of permanent magnet contactor with a flux-weakening control strategy', *J. Appl. Phys.*, 2011, **109**, (7), pp. 1–3, Art. ID. 07E707

[16] Fang, S., Lin, H., Ho, S.: 'Magnetic field analysis and dynamic characteristic prediction of ac permanent-magnet contactor', *IEEE Trans. Magn.*, 2009, **45**, (7), pp. 2990–2995

[17] Kawase, Y., Yamaguchi, T., Iwashita, K., *et al.*: '3-D finite element analysis of dynamic characteristics of electromagnet with permanent magnets', *IEEE Trans. Magn.*, 2006, **42**, (4), pp. 1339–1342

[18] Wang, X., Lin, H., Ho, S., *et al.*: 'Analysis of dynamic characteristics of permanent magnet contactor with sensorless displacement profile control', *IEEE Trans. Magn.*, 2010, **46**, (6), pp. 1633–1636

[19] Chen, D., Liu, Y., Ji, L., *et al.*: 'Simulation and analysis for a permanent contactor with and without current-feedback system', *IEICE Trans. Electron.*, 2009, **E92-C**, (8), pp. 1040–1044

[20] Bak, H.J., Ro, J.S., Chung, T.K., *et al.*: 'Characteristics analysis and design of a novel magnetic contactor for a 220 V/85 A', *IEEE Trans. Magn.*, 2013, **49**, (11), pp. 5498–5506

[21] Cho, D.J., Woo, D.K., Ro, J.S., *et al.*: 'Novel electromagnetic actuator using a permanent magnet and aninter-locking mechanism for a magnetic switch', *IEEE Trans. Magn.*, 2013, **49**, (5), pp. 2229–2232

[22] Espinosa, A., Ruiz, J.R., Morera, X.: 'A sensorless method for controlling the closure of a contactor', *IEEE Trans. Magn.*, 2007, **43**, (10), pp. 3896–3903

[23] Arand, S.J., Ardebili, M.: 'Multi-objective design and prototyping of a low cogging torque axial-flux PM generator with segmented stator for small-scale direct-drive wind turbines', *IET Electr. Power Appl.*, 2016, **10**, (9), pp. 889–899

[24] Shamlou, S., Mirsalim, M.: 'Design, optimisation, analysis and experimental verification of a new line-start permanent magnet synchronous shaded-pole motor', *IET Electr. Power Appl.*, 2013, **7**, (1), pp. 16–26